ELSEVIER

Solid State Ionics 116 (1999) 339–349

SOLID STATE IONICS

Defect cluster formation in M_2O_3-doped CeO_2

Licia Minervini, Matthew O. Zacate, Robin W. Grimes*

Department of Materials, Imperial College, London, SW7 2BP, UK

Received 30 June 1998; received in revised form 11 September 1998; accepted 22 September 1998

Abstract

Atomistic simulation calculations based on energy minimisation techniques have been used to study the energetics associated with M_2O_3 solution in CeO_2. Results show that the binding energy of an oxygen vacancy to one or two substitutional cations is a strong function of dopant cation radius; small dopant ions prefer to occupy first neighbour sites, large dopant ions prefer second neighbour sites. The crossover occurs at approximately Gd^{3+}, which also exhibits the smallest binding energy. These results are used to predict lattice parameter as a function of defect concentration and comparison is made to experimental values.

Keywords: Ceria; Defects; Atomistic simulation; Dopants; Solid solutions

PACS: 07.05.Tp; 61.72.-y

1. Introduction

Ceria doped with trivalent oxides has received particular attention because the resulting defect structure permits high oxygen ion conduction [1–4]. To fully exploit this effect it would be useful to establish the solution mechanism and determine the defect structures formed by the dopants in solution. In many cases a determining factor is the ionic size of the dopants. Therefore in this study, we develop a relationship between ionic radius and solution energy by modelling the systematic doping of ceria with M_2O_3, where M = Al, Cr, Ga, Fe, Sc, In, Y, Gd, Ce and La. We also focus on the effect that ion size has on defect cluster geometry and the results are used to calculate the overall change in lattice parameter as a function of defect concentration.

The body of information concerning doped ceria is vast and an exhaustive survey would be impractical. The aim here is to review a selection of studies investigating the effect of trivalent dopant ion size and defect association. Previous work, both experimental and theoretical, has attempted to rationalise the relationship between dopant size and conductivity in terms of the association of a single substitutional dopant cation to an oxygen vacancy forming the charged dimer, $(M'_{Ce}: V^{\cdot\cdot}_O)^{\cdot}$. The association of oxygen vacancies to dopant cations is significant because it reduces the ionic conductivity of the material; oxygen vacancies are very mobile but cations are not. We propose that, for completeness, the neutral trimer $(2M'_{Ce}: V^{\cdot\cdot}_O)^{\times}$ must also be considered. This is because the probability that a vacancy has more than one dopant ion close to it rapidly

*Corresponding author. Tel.: +0044-171-594-6730; fax: +044-171-584-3194; e-mail: r.w.grimes@ic.ac.uk

0167-2738/99/$ – see front matter
PII: S0167-2738(98)00359-2

increases with dopant concentration so that for concentrations beyond a few percent it is no longer meaningful to consider only the association of an oxygen vacancy to a single dopant ion.

In a detailed report on $Ce_{1-2x}Y_{2x}O_{2-x}$ Wang et al. [5] showed that in the dilute range ($x < 0.02$) charged dimers form. Gerhardt-Anderson and Nowick [6] extended this work to other CeO_2:M_2O_3 solid solutions, where $M = Sc^{3+}$, Y^{3+}, Gd^{3+} and La^{3+}, by using ac measurements and complex impedance analysis. They found that the maximum conductivity was obtained for Gd^{3+} doping. In addition, by analysing their results in terms of charged dimer clusters, they suggested that conductivity and dimer binding energy vary inversely with dopant cation radius. Kilner and Brook [7] concluded that the contribution of elastic strain energy to the binding energy of the dimer, due to size mismatch between host and dopant cations is large. Subsequent theoretical studies [8–10] emphasised the importance of defect clustering in the determination of the free carrier concentration, and hence conductivity, in the fluorite oxides.

2. Methodology

2.1. Simulation technique

Atomistic computer simulation techniques, based on energy minimisation with a Born-like description of the lattice [11] are used to generate the various structures. The procedures are based upon a description of lattice forces in terms of effective potentials. The perfect lattice is described by defining a unit cell which is repeated throughout space using periodic boundary conditions as defined by the usual crystallographic lattice vectors. The total energy of the crystal is minimised by allowing the ions in the unit cell and the lattice vectors to relax to zero strain.

We consider interactions due to long range Coulombic forces, which are summed using Ewald's method [12] and also short range forces, that are modelled using parameterised pair potentials, S_{ij}. The short range terms account for the electron cloud overlap and dispersion interactions which are negligible beyond a few lattice spacings. Thus, in order to reduce the computational time, the short range interactions are set to zero beyond 20 Å. In this study the Buckingham potential form was used,

$$S_{ij} = Ae^{(-r_{ij}/\rho)} - C/r_{ij}^6 \quad (1)$$

where A, ρ and C are three adjustable parameters. The values of these parameters (see Table 1) were chosen to reproduce the unit cell volumes of various oxides [13] and the perfect lattice properties of ceria (see Table 2). The consequence of this multi-structure parameter-fitting approach is that the potentials reflect the metal–oxygen and oxygen–oxygen interactions over a wider range of interatomic separations than would be the case if the fitting process were restricted to a single structure.

In addition to studying the perfect lattice, this approach can be used to predict how the lattice ions accommodate defect clusters. To do this the energy-minimised perfect lattice is partitioned into two regions: a spherical inner region, I, at the centre of which the defect is introduced, and an outer region, II, which extends to infinity. In region I, interactions are calculated explicitly so that the response of the lattice to the defect is modelled by relaxing the positions of all ions to zero force using a Newton–Raphson minimisation procedure.

The response of region II is treated using the Mott–Littleton approximation [14]. To ensure a smooth transition between regions I and II, we incorporate an interfacial region, IIa, in which ion displacements are determined via the Mott–Littleton approximation but in which interactions with ions in region I are calculated by explicit summation. In the present calculations, the radii of regions I and IIa

Table 1
Short-range pair potential parameters

Species	A (eV)	ρ (Å)	C (e VÅ^6)	Reference
O^{2-}–O^{2-}	9547.96	0.2192	32.0	[13,24,38–41]
Al^{3+}–O^{2-}	1725.20	0.28971	0.0	[38]
Cr^{3+}–O^{2-}	1204.18	0.3165	0.0	[24]
Ga^{3+}–O^{2-}	1625.72	0.3019	0.0	[40]
Fe^{3+}–O^{2-}	1414.60	0.3128	0.0	[26]
Sc^{3+}–O^{2-}	1575.85	0.3211	0.0	[13]
In^{3+}–O^{2-}	1495.65	0.3327	4.33	[41]
Y^{3+}–O^{2-}	1766.40	0.33849	19.43	[13]
Gd^{3+}–O^{2-}	1885.75	0.3399	20.34	–
Ce^{3+}–O^{2-}	2010.18	0.3449	23.11	–
La^{3+}–O^{2}	2088.79	0.3460	23.25	–
Ce^{4+}–O^{2-}	1809.68	0.3547	20.40	[42]

Table 2
Comparison of predicted and experimental lattice properties

	Prediction	Experimental	Reference
$r_{lattice}$ (Å)	5.410	5.411	[43]
$E_{lattice}$ (eV)	−105.65	−99.77	[44]
ϵ_0	18.62	18.6 − 20.0	[42]
		24.5	[45]
ϵ_∞	5.88	4.0	[42]
		5.31	[45]
c_{11} (10^{11} dyne/cm^2)	55.45	40.3	[46]
c_{12} (10^{11} dyne/cm^2)	12.46	10.5	[46]
c_{44} (10^{11} dyne/cm^2)	12.31	6.0	[46]

were 11.6 Å and 31.9 Å, respectively. Region sizes were chosen to be large enough to ensure that no appreciable change in defect formation energy occurred if the region sizes were increased further.

In all calculations, O^{2-} and Ce^{4+} ions are treated as polarisable using the shell model [15]. This consists of a massless shell with charge $X|e|$ that is allowed to move with respect to a massive core of charge $Y|e|$; the overall charge state of each oxygen ion is therefore equal to $(X+Y)|e|$. The core and shell charges are connected by an isotropic harmonic spring force constant of k (see Table 3). Displacement of the shell relative to the core gives a good description of electronic polarisation. The cerium shell model was included to ensure that the predicted dielectric constant of CeO_2 was in agreement with the experimental values. This is important because the predicted dielectric constant is used in the Mott–Littleton approximation. We also considered the effect of introducing shell models, derived from experimental values of ϵ_0 for La_2O_3 and Gd_2O_3 [16], for the large cations Gd^{3+} and La^{3+}. However, this had no effect on the predicted defect binding energies and the parameters are therefore not reported.

This type of calculation is usually referred to as 'static' since lattice vibration entropy contributions are not included in the model. Furthermore configurational entropy is also ignored. The energies calculated are therefore enthalpies and relate, via the quasi-harmonic approximation, to the temperature of the lattice to which the potential parameters were fitted, in this case, room temperature. Entropy contributions are usually small at room temperature, nonetheless this introduces some uncertainty into any analysis that relies on enthalpies as the sole way of determining defect structures. This is partly why here we choose to predict lattice parameter and compare this with experiment, rather than rely only on defect enthalpies. For further details of the computational methods see [17–21]. In all cases, calculations were carried out using the CASCADE[1] code [22].

Table 3
Shell parameters

Species	$Y(e)$	k (eV Å^{-2})	Reference
O^{2-}	−2.04	6.3	[13,24,38–41]
Ce^{4+}	−0.20	177.84	[42]

2.2. Defective unit cell volumes

The Mott–Littleton defect calculations can also be used to predict lattice volumes. The defect relaxation volume, ν, can be calculated from:

$$\nu = -K_T V_C \left(\frac{\partial f_v}{\partial v_T} \right) \quad (2)$$

where K_T is the isothermal compressibility and V the unit cell volume [23,24]. $((\partial f_v)/(\partial v))_T$ is the change, at constant temperature, in the Helmholtz defect formation energy as a function of the change in the unit cell volume. Given the defect relaxation volume, the unit cell volume can be determined from:

Unit cell volume	= Σ	Volume of defects	×	Concentration of defects	+	Perfect unit cell volume

[1] Cray Automated System for the Calculation of Defect Energies.

Clearly, such predictions totally neglect any effects of long range defect–defect interactions. However, as is seen in the present study and as recently demonstrated by Vyas et al. [25] for Al_2O_3 solutions in MgO and by Minervini and Grimes for $Fe_{1-x}O$ [26], such predictions do not significantly deviate from equivalent LUC calculations until surprisingly high defect concentrations are reached.

3. Results and discussion

3.1. Intrinsic disorder

There are three possible intrinsic disorder reactions in ceria:

$$\text{Schottky } Ce_{Ce}^{\times} + 2O_O^{\times} \leftrightarrow V_{Ce}'''' + 2V_O^{\cdot\cdot} + CeO_2 \quad \Delta E = 3.53 \text{ eV} \tag{3}$$

$$\text{Cation Frenkel } Ce_{Ce}^{\times} \leftrightarrow Ce_i^{\cdot\cdot\cdot\cdot} + V_{Ce}'''' \quad \Delta E = 11.11 \text{ eV} \tag{4}$$

$$\text{Anion Frenkel } O_O^{\times} \leftrightarrow O_i'' + V_O^{\cdot\cdot} \quad \Delta E = 3.2 \text{ eV} \tag{5}$$

From the reaction energies, ΔE, it is evident that the predominant disorder mechanism is Anion Frenkel. Simple mass action analysis based on these values indicates that the concentration of defects on the oxygen sublattice will be much greater than that on the cation sublattice. This result is in accordance with the experimental observations [27–29].

3.2. Extrinsic disorder

When an aliovalent solute is dissolved in a solid, the crystal lattice must compensate for the resulting charge imbalance. For example, M_2O_3 can be incorporated into CeO_2 via three mechanisms all of which are related by the intrinsic disorder reactions:

$$M_2O_3 \overset{CeO_2}{\leftrightarrow} 2M_{Ce}' + V_O^{\cdot\cdot} + 3O_O^{\times} \tag{6}$$

$$2M_2O_3 \overset{CeO_2}{\leftrightarrow} 3M_{Ce}' + M_i^{\cdot\cdot\cdot} + 6O_O^{\times} \tag{7}$$

$$Ce_{Ce}^{\times} + 2O_O^{\times} + 2M_2O_3 \overset{CeO_2}{\leftrightarrow} 4M_{Ce}' + Ce_i^{\cdot\cdot\cdot\cdot} + 8O_O^{\times} \tag{8}$$

These will be referred to as vacancy compensation [Eq. (6)], dopant interstitial compensation [Eq. (7)] and cerium interstitial compensation [Eq. (8)] respectively. However, if we assume thermodynamic equilibrium and evoke one or more of the intrinsic defect reactions (i.e. Eqs. (3) and (4) or Eq. (5)) we can easily show that there is, in fact, only one independent compensation mechanism. Nevertheless, as the formation energies of the intrinsic defects are high, the assumption of thermodynamic equilibrium may not be justified. We have therefore obtained energies for all three reactions. Our results show (see Fig. 1) that vacancy compensation is clearly the favourable solution mechanism for large cations (see Table 4). For the smallest dopant cations some compensation via dopant interstitials may occur, although these will be minority defects. Furthermore, if we include defect cluster formation in the model the difference in these reaction energies becomes very small, but only for the smallest cations, and should be considered in further work. Nevertheless, since this study is primarily concerned with larger cations, reactions other than oxygen vacancy compensation will not be discussed further.

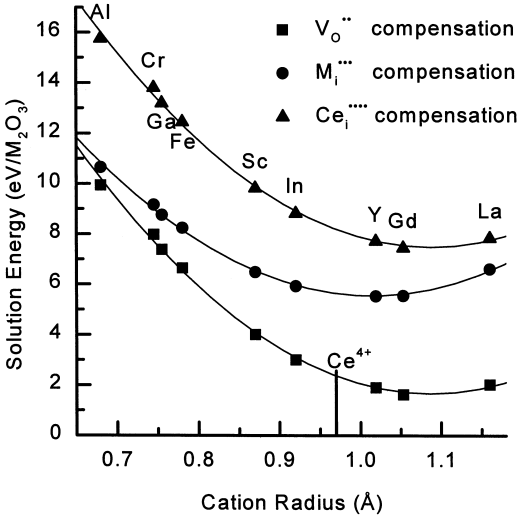

Fig. 1. Solution energies for the incorporation of M_2O_3 into CeO_2 assuming isolated point defects.

Table 4
Ionic radii for VIII-coordinated ions after Shannon [47]

Ion	Radius (Å)
Al^{3+}	0.693[a]
Cr^{3+}	0.752[a]
Ga^{3+}	0.760[a]
Fe^{3+}	0.780
Sc^{3+}	0.87
In^{3+}	0.92
Ce^{4+}	0.97
Y^{3+}	1.019
Gd^{3+}	1.053
Ce^{3+}	1.143
La^{3+}	1.160

[a] Extrapolated using octahedral ionic radii.

3.2.1. Formation of defect clusters: $(M'_{Ce}: V_O^{\cdot\cdot})^{\cdot}$

The substitution of trivalent dopant cations for Ce^{4+} is accompanied by the formation of an oxygen vacancy for every two M^{3+} ions. A simplistic interpretation of the defect structure postulates that, at least for low dopant concentrations, associated pairs, $(M'_{Ce}: V_O^{\cdot\cdot})^{\cdot}$, and isolated M'_{Ce} are randomly distributed throughout the host matrix. This model has been used to illustrate various properties of these solid solutions, such as conductivity [30] and dielectric relaxation [31]. Models for conductivity assume that the mobile oxygen vacancies move through the lattice becoming associated to M^{3+} substitutional ions which are essentially at fixed points.

When considering the formation of these associates it is important to determine which configurations are most stable. A measure of cluster stability is the binding energy, *BE*, defined as the difference between the sum of the formation enthalpies of the defect cluster's component point defects and the formation enthalpy of the defect cluster:

$$BE_{\text{cluster}} = \left[\sum_{\text{components}} E_{\text{defect}}\right] - E_{\text{cluster}}. \qquad (9)$$

A positive binding energy indicates a preference for the cluster over its components, therefore higher binding energies denote greater stability. Fig. 2 dimer shows the binding energy of a substitutional dopant cation to an oxygen vacancy at first, second and third neighbour sites. Fig. 3 illustrates these positions within the fluorite unit cell. For cations smaller than Gd^{3+} it is energetically favourable for the vacancy to be in a first neighbour position with respect to the substitutional ion, while cations larger than Gd^{3+} prefer second neighbour vacancies. The crossover point, at approximately the Gd^{3+} cation radius, coincides with the minimum binding energy.

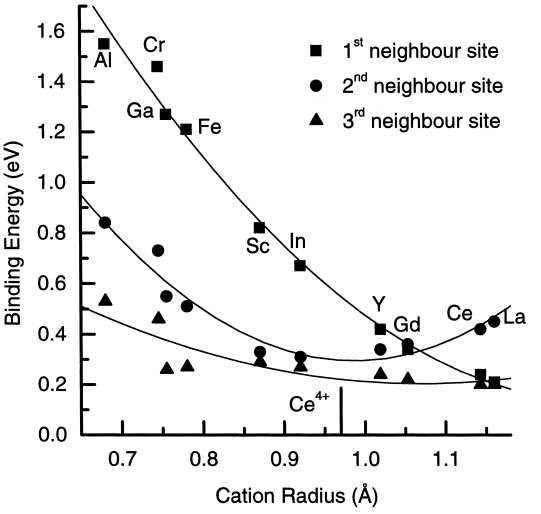

Fig. 2. Binding energies of M^{3+} dopant cations to an oxygen vacancy.

In a previous study Pryde et al. [32] found that an In^{3+} substitutional ion will exhibit essentially the same binding energy to an oxygen vacancy independently of whether the two are first or second neighbours. This result was explained in terms of a

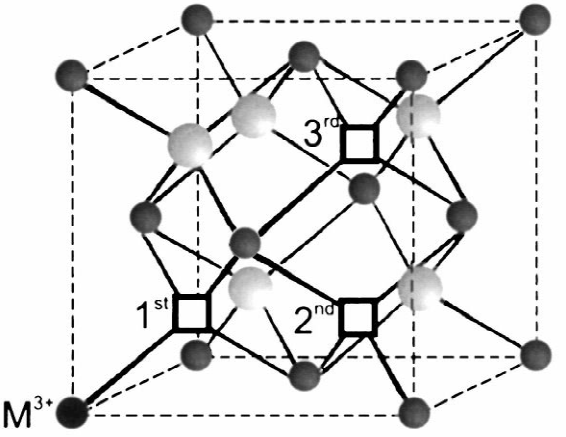

Fig. 3. First, second and third neighbour oxygen ion sites with respect to a substitutional ion.

competitive effect between Coulombic and relaxation energies. Coulombic attraction between the vacancy and the dopant substitutional ion favours the first neighbour site, while the relaxation energy favours the second neighbour site. This is because, in the second neighbour site configuration, the Ce^{4+} ion adjacent to the oxygen vacancy can relax away from the effectively positive vacancy without moving away from the effectively negative substitutional ion. Pryde et al. proposed that these effects cancel to yield equivalent binding energies for the In^{3+} substitutional ion. In the present work we find that the effects only cancel when the dopant ionic radius is $\approx$1.05 (i.e. that of Gd^{3+} which is 15% greater than the ionic radius of In^{3+}). The reason for the discrepancy is that the potential set used here was derived in a fully consistent manner whereas the potentials employed by Pryde et al. were derived independently. We now realise that this can cause errors and potentials must be derived consistently if reliable results are to be achieved. Nevertheless, analysis of relaxed ion positions shows that the rationale put forth in this previous study, albeit in an extended form, remains valid.

In order to explain the trends shown in Fig. 2 a third factor is required concerning ions' sizes. Thus the preference for the oxygen vacancy to reside in a first or second neighbour site is a consequence of three factors:

- Coulomb interactions between charged defects (i.e. $V_O^{\cdot\cdot}$ and $M_{Ce}^{\prime}$). This always favours the first neighbour position.
- Relaxation of the lattice. This is the crystallographic effect, driven primarily by Coulombic considerations, described by Pryde et al. and always favours the second neighbour position.
- Modifications to the relaxation of the lattice due to ion size effects. In essence, these arise because small ions generally prefer lower coordination.

The overall effect of lattice relaxation is illustrated in Fig. 4 which shows the relaxation energy as a function of ion size for both the first and second neighbour configurations. There are several points to note from this. First, the relaxation energy is always greater for the second neighbour site, this is due to the Pryde crystallographic relaxation effect. Second,

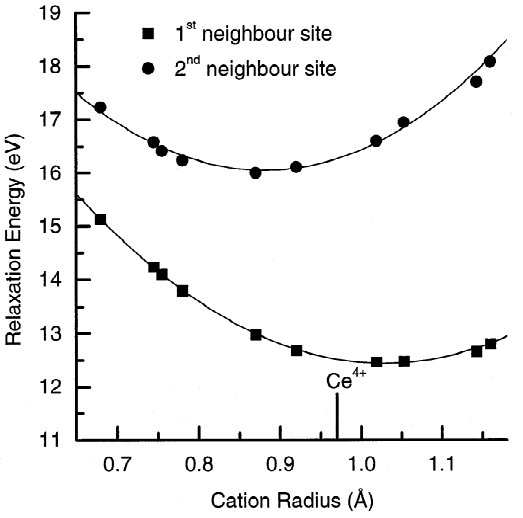

Fig. 4. Effect of dopant ion size on lattice relaxation for both first and second neighbour cluster configurations.

the relaxation energy associated with the first neighbour configuration is much less for large ions. This is a consequence of the way in which the first coordination anion shell surrounding the impurity relaxes to produce a highly distorted VII-fold environment where four of the oxygen ions are closer to the impurity than the other three. In essence, this is a manifestation of small cations attempting to form in pseudo-tetrahedral coordination. Distortion of the oxygen polyhedron into two subshells around small cations (specifically Sc^{3+}) was predicted by the computer simulations of Cormack et al. [33]. Recently, these calculations were confirmed using X-ray absorption spectroscopy techniques by Li et al. [34] who found that the environment surrounding the Sc^{3+} ion is VII-fold with two different Sc-O distances. However, this relaxation mode is only possible for small dopants and becomes impractical for large cations. Consequently, the total relaxation energy decreases with ion size.

Finally, Fig. 4 shows that the relaxation energy associated with the second neighbour configuration is slightly larger for large cations. This is because larger cations are better able to take advantage of the increase in volume associated with the second neighbour relaxation mode. However, we also find that small cations move off-centre in the VIII-coordinate space delimited by the anions.

3.2.2. Formation of defect clusters: $(2M'_{Ce}: V_O^{\cdot\cdot})^{\times}$

For concentrated solutions (x in $Ce_{1-2x}M_{2x}O_{2-x}$> 0.1) the probability of finding an isolated dopant (i.e. one with no other dopant ions in first or second neighbour positions) is necessarily small [30]. Consequently, there is a need to consider the case where an oxygen vacancy is associated with two cations, forming a neutral trimer. The situation becomes more complex than when dealing with simple pairs, because the number of possible defect geometries increases. In total there are sixteen unique combinations involving first and second neighbour cation interactions with the oxygen vacancy. As illustrated in Fig. 5 the binding energy results obtained upon consideration of neutral trimers is qualitatively similar to the picture depicted by the charged dimers. Thus we see again, that small cations prefer first neighbour positions, that large cations favour second neighbour sites and that the intersection of these preferences results in a minimum binding energy at approximately the Gd^{3+} cation radius. This explains why simple models, that only consider dimers, are successful in interpreting the behaviour of materials where the dopant concentrations are far greater than those where the use of isolated charged defects seems justified.

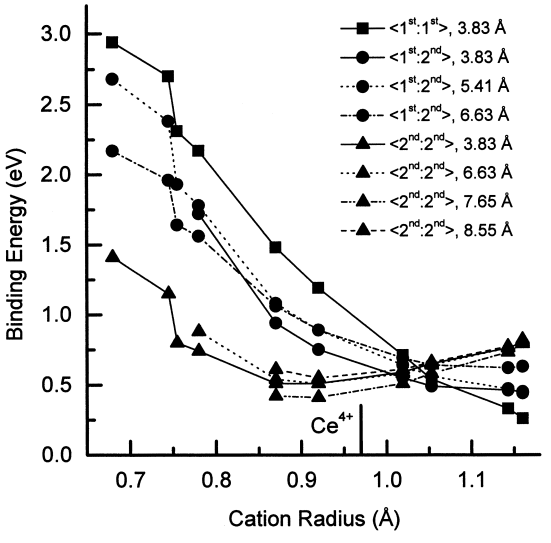

Fig. 5. Binding energy of $(2M'_{Ce}: V_O^{\cdot\cdot})^{\times}$ clusters. The legend specifies <1st: 1st> i.e. both cations in first neighbour sites with respect to the oxygen vacancy, <1st: 2nd> and <2nd: 2nd> configurations. The various <1st: 2nd> and <2nd: 2nd> configurations are distinguished by the distance separating the dopant cations. Although there are two distinct configurations for each dopant cation separation, these are energetically similar and only the more stable configuration is reported.

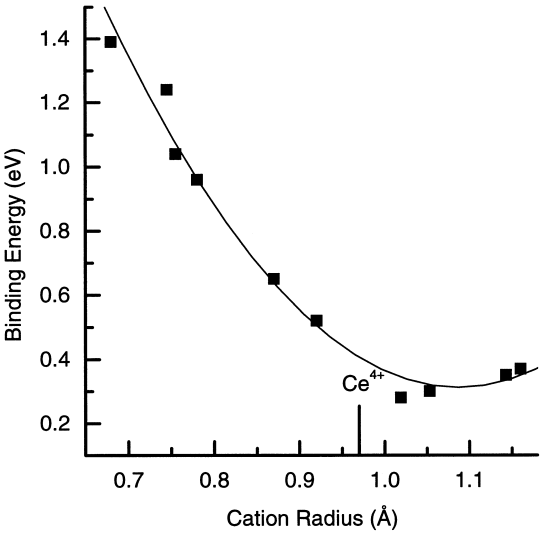

Fig. 6. Binding energy of a M'_{Ce} dopant cation to a $(M'_{Ce}: V_O^{\cdot\cdot})^{\cdot}$ cluster. For each cation the most stable configuration is considered.

The local structure around the dopant cations found by X-ray absorption studies [34] suggests that the defect structure of 5 mol% Sc_2O_3-doped ceria solutions (corresponding to $x \approx 0.056$) consists of a combination of dimers and isolated cations, while the defect structure of 10 mol% Sc_2O_3-doped ceria (corresponding to $x = 0.125$) can be described by trimers. However, these studies did not find further clustering of dimers into trimers for solutions containing up to 10 mol% Gd_2O_3 dopant. Although, this is consistent with the present results, which show that the binding energy of a second cation to a dimer is much smaller in Gd-doped ceria than in Sc-doped ceria (see Fig. 6), it is hard to understand geometrically how at a 10 mol% dopant level a dimer will remain isolated from a second Gd^{3+} ion, unless the definition of trimer in the previous study assumed explicitly only first neighbour configurations.

3.3. Lattice parameter variation

To understand better the effect of M_2O_3 solution in a CeO_2 matrix and to test the validity of our

model directly against experiment, the variation of lattice parameter with solute concentration was investigated. There are experimental data available for lattice parameter change with concentration for four of the dopants considered in this study [6,35,36]. These data will be compared to the predicted lattice parameter change assuming different defect models calculated via the $((\partial fv/\partial v))_T$ defect volume methodology [23,24].

Figs. 7–10 show the predicted lattice parameters as a function of concentration for M_2O_3:CeO_2 solid solutions, where M = Sc, Y, Gd and La. The relevant experimental data is included for comparison. For each dopant three models are shown, those based on isolated defects, the most energetically stable dimer configuration and the most energetically stable trimer configuration. However, it was found that the lattice parameter variation with concentration is relatively independent of defect model and defect cluster geometry. Furthermore, the differences between the three defect models are on the order of the spread in the experimental data, such that this analysis of lattice parameter variation does not allow us to exclude any of the models although it does provide a good test of the methodology.

The lattice parameter results will be discussed beginning with La^{3+} solution (see Fig. 7). In this case, our predictions can be compared to three sets of experimental results, all of which are in good agreement with each other for values of x in $Ce_{1-2x}La_{2x}O_{2-x}$ less than ≈ 0.15. Within this region, our predicted values are consistent with these experiments. For larger values of x, the experimental data of Bevan & Summerville deviates significantly from

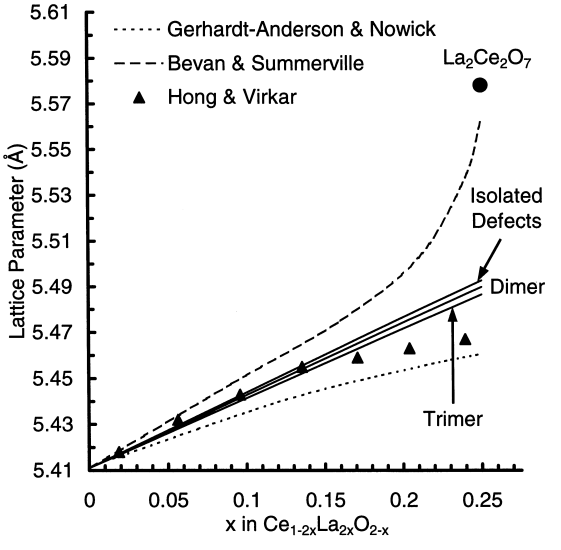

Fig. 7. Dependence of lattice parameter on dopant concentration in La_2O_3:CeO_2 solutions.

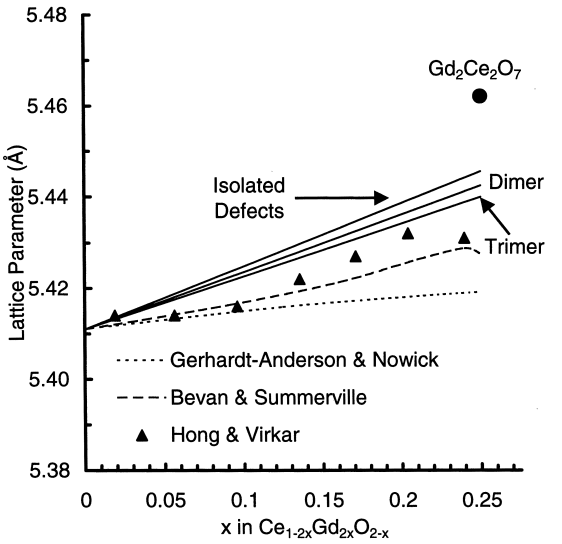

Fig. 8. Dependence of lattice parameter on dopant concentration in Gd_2O_3:CeO_2 solutions.

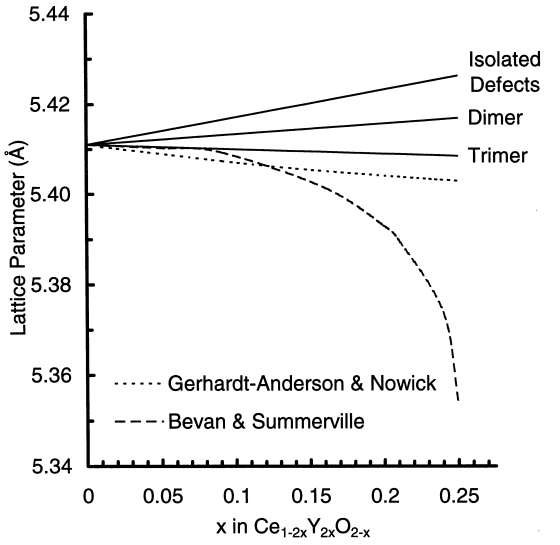

Fig. 9. Dependence of lattice parameter on dopant concentration in Y_2O_3:CeO_2 solutions.

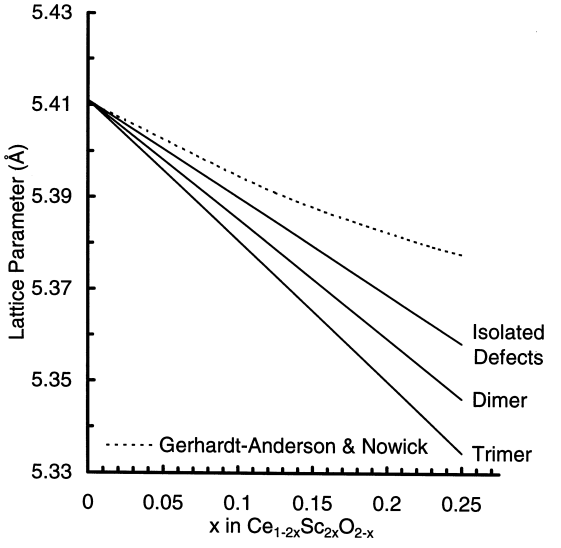

Fig. 10. Dependence of lattice parameter on dopant concentration in Sc_2O_3:CeO_2 solutions.

that of Hong and Virkar, Gerhardt–Anderson and Nowick and from our predicted values. To investigate further the cause of this deviation, we carried out a perfect lattice calculation at $x=0.25$ which corresponds to the stoichiometric composition of $La_2Ce_2O_7$. In this calculation, the oxygen vacancies were assumed to exhibit an ordering found in the cubic pyrochlore structure. The resulting lattice energy of this pyrochlore was found to be stable with respect to decomposition and its lattice parameter, after relaxation, is shown in Fig. 7 as a single point.

$$La_2O_3 + 2CeO_2 \rightarrow La_2Ce_2O_7 \quad \Delta E = -1.06 \text{ eV} \tag{10}$$

The convergence of the data of Bevan and Summerville to the predicted pyrochlore structure seems to imply that the experimental conditions of Bevan and Summerville were conducive to a defect ordering corresponding essentially to that of a pyrochlore, whereas those of Hong and Virkar and Gerhardt–Anderson and Nowick were not. However, this conclusion is tentative and more studies are necessary before definite conclusions may be drawn.

In the case of Gd^{3+} solution (see Fig. 8) our predictions can again be compared to three sets of compatible experimental results. Throughout the range of dopant concentrations our predicted values for all three defect models yield approximately the same deviation, which is consistent with experiment. In this case, formation of the associated pyrochlore, $Gd_2Ce_2O_7$, is not predicted to show a significant energy gain.

$$Gd_2O_3 + 2CeO_2 \rightarrow Gd_2Ce_2O_7 \quad \Delta E = -0.04 \text{ eV} \tag{11}$$

However the possibility of some partial ordering of defects into a pyrochlore type arrangement cannot be totally excluded as the lattice parameter of $Gd_2Ce_2O_7$ is consistent with experimental data (see Fig. 8).

With regard to dilute solutions of Y-doped ceria our predictions (see Fig. 9) show almost no change in lattice parameter with defect concentration and are thus compatible with both sets of available experimental data. However, at higher concentrations ($x>0.15$) the data of Bevan and Summerville shows a strong deviation which cannot be understood in terms of pyrochlore formation as again this structure is predicted to be unstable.

$$Y_2O_3 + 2CeO_2 \rightarrow Y_2Ce_2O_7 \quad \Delta E = 1.82 \text{ eV} \tag{12}$$

The predicted instability of $Y_2Ce_2O_7$ is supported by the cation radius ratio (Y:Ce) which is unfavourable to the formation of a pyrochlore structure [37].

Only the study by Gerhardt–Anderson and Nowick included data on Sc-doped ceria. On the basis of this data our predictions (see Fig. 10) are in agreement.

Overall, as a function of concentration, solution of M_2O_3 in CeO_2 results in a variety of changes in lattice parameter. The results presented here show that the methodology, and in particular the interatomic potentials we employ are able to reproduce experimental variations accurately.

4. The conclusions

The results are consistent with M_2O_3 solution in CeO_2 via an oxygen vacancy compensation mechanism. The resulting charged defects are attracted to one another, and exhibit binding energies which are a strong function of the dopant ion size. The atomic

arrangement of the defects in the cluster are controlled by a combination of Coulombic attraction and crystallographic relaxation effects, the latter being dependent on ion size. Thus small dopants show greatest binding energies when the oxygen vacancy is in a first neighbour site and large dopants prefer the oxygen vacancy to be in a second neighbour site. Furthermore, the crossover point occurs for the dopant that exhibits the lowest binding energy, i.e. Gd^{3+} which exhibits the highest ionic conductivity of all doped ceria materials.

Although the same conclusions can be drawn from the simple dimer defect model, clearly trimer clusters cannot be ignored. Trimers exhibit high binding energies, particularly when the size misfit of the dopant to the matrix is large. Additionally, at high dopant concentrations it is inconceivable that simple pairs will remain isolated.

Finally, we find that the variation of lattice parameter with defect concentration is not strongly dependent on defect model (i.e. isolated defects, dimer or trimer) or on defect cluster geometry. Furthermore, the results show that our model reproduces experimental data; in particular, that doping with La_2O_3 and Gd_2O_3 gives rise to an expansion of the lattice as a function of defect concentration, Sc_2O_3 doping leads to a contraction of the lattice but that Y_2O_3-doped CeO_2 shows negligible change in lattice parameter even at high defect concentrations.

Acknowledgements

Licia Minervini would like to thank Los Alamos National Laboratory for financial support. Informative discussions with Professor J.A. Kilner are gratefully acknowledged. Some computing facilities were provided through EPSRC grant number GR/L86821.

References

[1] H.L. Tuller, A.S. Nowick, J. Electrochem. Soc. 122 (1975) 255.
[2] T. Kudo, H. Obayashi, J. Electrochem. Soc. 123 (1976) 415.
[3] R.T. Dirstine, R.N. Blumenthal, T.F. Kuech, J. Electrochem. Soc. 126 (1979) 264.
[4] K. Eguchi, H. Yahiro, H. Arai, Solid State Ionics 36 (1989) 71.
[5] D.H. Wang, D.S. Park, J. Griffith, A.S. Nowick, Solid State Ionics 2 (1981) 95.
[6] R. Gerhardt-Anderson, A.S. Nowick, Solid State Ionics 5 (1981) 547.
[7] J.A. Kilner, R.J. Brook, Solid State Ionics 6 (1982) 237.
[8] J.A. Kilner, C.D. Waters, Solid State Ionics 6 (1982) 253.
[9] V. Butler, C.R.A. Catlow, B.E.F. Fender, J.H. Harding, Solid State Ionics 8 (1983) 109.
[10] J.A. Kilner, Solid State Ionics 8 (1983) 201.
[11] M. Born, Atomtheorie des Festen Zustandes, Teubner Leipzig, 1923.
[12] P.P. Ewald, Ann. Physik 64 (1921) 253.
[13] R.W. Grimes, G. Busker, M.A. McCoy, A. Chroneos, J.A. Kilner, Ber. Bunsenges. Phys. Chem. 101 (1997) 1204.
[14] N.F. Mott, M.J. Littleton, Trans. Farad. Soc. 34 (1932) 485.
[15] B.G. Dick, A.W. Overhauser, Phys. Rev. 112 (1958) 90.
[16] D.J. Jlett, M.S. Islam, J. Chem. Soc. Faraday Trans. 89 (1993) 3822.
[17] C.R.A. Catlow, W.C. Mackrodt (Eds.), Computer Simulation of Solids, Springer-Verlag Berlin, 1982.
[18] C.R.A. Catlow, A.M. Stoneham (Eds.), (special issue), J. Chem. Soc. Farad. Trans. 85(5) (1989).
[19] A.H. Harker, R.W. Grimes, Mol. Sim. 4(5) (1990).
[20] A.H. Harker, R.W. Grimes, (special issue), Mol. Sim. 5(2) (1990).
[21] C.R.A. Catlow (Ed.), (special issue), J. Mater. Chem. 4 (1994).
[22] M. Leslie, DL/SCJ/TM31T, Technical report SERC Daresbury Laboratory, 1982.
[23] C.R.A. Catlow, J. Corish, P.W.M. Jacobs, A.B. Lidiard, J. Phys C. 14 (1981) L121.
[24] R.W. Grimes, D.J. Binks, A.B. Lidiard, Phil. Mag. 72 (1995) 651.
[25] S. Vyas, R.W. Grimes, D.J. Binks, F. Rey, J. Phys. Chem. Solids 58 (1997) 1619.
[26] L. Minervini, R.W. Grimes, J. Phys. Chem. Solids (in press).
[27] H.L. Tuller, A.S. Nowick, J. Phys. Chem. Solids 38 (1977) 859.
[28] H.L. Tuller, A.S. Nowick, J. Electrochem. Soc 126 (1979) 209.
[29] E.K. Chang, R.N. Blumenthal, J. Solid State Chem. 72 (1988) 330.
[30] G.E. Murch, A.S. Nowick (Eds.), Diffusion in Crystalline Solids, ch. 3, Academic Press, Orlando, FL, 1984.
[31] D.Y. Wang, A.S. Nowick, Solid State Ionics 5 (1981) 551.
[32] A.K.A. Pryde, S. Vyas, R.W. Grimes, J.A. Gardner, R. Wang, Phys. Rev. B 52 (1995) 13214.
[33] A.N. Cormack, C.R.A. Catlow, A.S. Nowick, J. Phys. Chem. Solids 50 (1989) 177.
[34] P. Li, I.-W. Chen, J.E. Penner-Hahn, T.Y. Tien, J. Am. Ceram. Soc. 74 (1991) 958.
[35] D.J.M. Bevan, B. Summerville. Mixed rare earth oxides, in: K.A. Gschneidner, Jr., L. Eyring (Eds.), Handbook of the Physics and Chemistry of Rare Earths, vol. 3, Non-metallic Compound – I, Elsevier Science Publishers, 1979, p. 401–524.

[36] S.J. Hong, A.V. Virkar, J. Am. Ceram. Soc. 78 (1995) 433.
[37] M.A. Subramanian, G. Aravamudan, G.V. Subba Rao, Prog. Solid. State Chem. 15 (1983) 55.
[38] R.W. Grimes, J. Am. Ceram. Soc. 77 (1994) 378.
[39] M.A. McCoy, R.W. Grimes, W.E. Lee, Phil. Mag. A 75 (1997) 833.
[40] S.P. Chen, M. Yan, R.W. Grimes, S. Vyas, Ceramic Trans. 69 (1997) 129.
[41] M.A. McCoy, R.W. Grimes, W.E. Lee, Phil. Mag. A 76 (1997) 1187.
[42] S. Vyas, R.W. Grimes, D.H. Gay, A.L. Rohl, J. Chem. Soc. Faraday Trans. 94 (1998) 427.
[43] R.W.G. Wyckoff, Crystal Structures, vol. 1, 2nd ed., John Wiley and Sons, Inc., New York, 1963.
[44] R.C. Weast, (Ed.), CRC Handbook of Chemistry and Physics, 65th ed., CRC Press, Inc., Boca Raton, FL, 1984–1985.
[45] S. Mochisuki. Phys. Stat. Sol. B 114 (1982) 189.
[46] A. Nakajima, A. Yoshihara, M. Ishigame, Phys. Rev. B 50 (1994) 13297.
[47] R.D. Shannon, Acta Cryst. A32 (1976) 751.